

Visualization of prostatic nerves by polarization-sensitive optical coherence tomography

YEOREUM YOON,¹ SEUNG HWAN JEON,² YONG HYUN PARK,² WON HYUK JANG,³ JI YOUL LEE,² AND KI HEAN KIM^{1,3,*}

¹Department of Mechanical Engineering, Pohang University of Science and Technology, San 31, Hyoja-dong, Nam-gu, Pohang, Gyeongbuk 790-784, South Korea

²Department of Urology, College of Medicine, The Catholic University of Korea, 505 Banpo-dong, Seocho-gu, Seoul 137-040, South Korea

³Division of Integrative Biosciences and Biotechnology, Pohang University of Science and Technology, San 31, Hyoja-dong, Nam-gu, Pohang, Gyeongbuk 790-784, South Korea

*kiheankim@postech.ac.kr

Abstract: Preservation of prostatic nerves is critical to recovery of a man's sexual potency after radical prostatectomy. A real-time imaging method of prostatic nerves will be helpful for nerve-sparing radical prostatectomy (NSRP). Polarization-sensitive optical coherence tomography (PS-OCT), which provides both structural and birefringent information of tissue, was applied for detection of prostatic nerves in both rat and human prostate specimens, *ex vivo*. PS-OCT imaging of rat prostate specimens visualized highly scattering and birefringent fibrous structures superficially, and these birefringent structures were confirmed to be nerves by histology or multiphoton microscopy (MPM). PS-OCT could easily distinguish these birefringent structures from surrounding other tissue compartments such as prostatic glands and fats. PS-OCT imaging of human prostatectomy specimens visualized two different birefringent structures, appearing fibrous and sheet-like. The fibrous ones were confirmed to be nerves by histology, and the sheet-like ones were considered to be fascias surrounding the human prostate. PS-OCT imaging of human prostatectomy specimens along the perimeter showed spatial variation in the amount of birefringent fibrous structures which was consistent with anatomy. These results demonstrate the feasibility of PS-OCT for detection of prostatic nerves, and this study will provide a basis for intraoperative use of PS-OCT.

©2016 Optical Society of America

OCIS codes: (170.4500) Optical coherence tomography; (260.5430) Polarization; (230.5440) Polarization-selective devices; (180.4315) Nonlinear microscopy; (170.3880) Medical and biological imaging; (170.7230) Urology.

References and links

1. P. C. Walsh and P. J. Donker, "Impotence following radical prostatectomy: insight into etiology and prevention," *J. Urol.* **128**(3), 492–497 (1982).
2. F. Montorsi, A. Salonia, N. Suardi, A. Gallina, G. Zanni, A. Briganti, F. Deho', R. Naspro, E. Farina, and P. Rigatti, "Improving the preservation of the urethral sphincter and neurovascular bundles during open radical retropubic prostatectomy," *Eur. Urol.* **48**(6), 938–945 (2005).
3. T. M. Kessler, F. C. Burkhard, and U. E. Studer, "Nerve-sparing open radical retropubic prostatectomy," *Eur. Urol.* **51**(1), 90–97 (2007).
4. A. Takenaka, G. Murakami, H. Soga, S. H. Han, Y. Arai, and M. Fujisawa, "Anatomical analysis of the neurovascular bundle supplying penile cavernous tissue to ensure a reliable nerve graft after radical prostatectomy," *J. Urol.* **172**(3), 1032–1035 (2004).
5. A. Lunacek, C. Schwentner, H. Fritsch, G. Bartsch, and H. Strasser, "Anatomical radical retropubic prostatectomy: 'curtain dissection' of the neurovascular bundle," *BJU Int.* **95**(9), 1226–1231 (2005).
6. A. J. Costello, M. Brooks, and O. J. Cole, "Anatomical studies of the neurovascular bundle and cavernosal nerves," *BJU Int.* **94**(7), 1071–1076 (2004).
7. Y. H. Park, C. W. Jeong, and S. E. Lee, "A comprehensive review of neuroanatomy of the prostate," *Prostate Int.* **1**(4), 139–145 (2013).
8. J. Walz, A. L. Burnett, A. J. Costello, J. A. Eastham, M. Graefen, B. Guillonnet, M. Menon, F. Montorsi, R. P. Myers, B. Rocco, and A. Villers, "A critical analysis of the current knowledge of surgical anatomy related to optimization of cancer control and preservation of continence and erection in candidates for radical prostatectomy," *Eur. Urol.* **57**(2), 179–192 (2010).
9. C. Eichelberg, A. Erbersdobler, U. Michl, T. Schlomm, G. Salomon, M. Graefen, and H. Huland, "Nerve distribution along the prostatic capsule," *Eur. Urol.* **51**, 105–110 (2007).

10. K. D. Sievert, J. Hennenlotter, I. Laible, B. Amend, D. Schilling, A. Anastasiadis, U. Kuehs, U. Nagele, and A. Stenzl, "The periprostatic autonomic nerves--bundle or layer?" *Eur. Urol.* **54**(5), 1109–1117 (2008).
11. B. J. Gantz, "Intraoperative facial nerve monitoring," *Am. J. Otol.* **6**, 58–61 (1985).
12. J. M. Kartush, J. K. Niparko, S. C. Bledsoe, M. D. Graham, and J. L. Kemink, "Intraoperative facial nerve monitoring: a comparison of stimulating electrodes," *Laryngoscope* **95**(12), 1536–1540 (1985).
13. Y. Kaiho, H. Nakagawa, H. Saito, A. Ito, S. Ishidoya, S. Saito, and Y. Arai, "Nerves at the ventral prostatic capsule contribute to erectile function: initial electrophysiological assessment in humans," *Eur. Urol.* **55**(1), 148–155 (2009).
14. S. Rai, A. Srivastava, P. Sooriakumaran, and A. Tewari, "Advances in imaging the neurovascular bundle," *Curr. Opin. Urol.* **22**(2), 88–96 (2012).
15. A. D. Gupta and M. Han, "Imaging guidance in minimally invasive prostatectomy," *Urol. Oncol.* **29**(3), 343–346 (2011).
16. K. Ponnusamy, J. M. Sorger, and C. Mohr, "Nerve mapping for prostatectomies: novel technologies under development," *J. Endourol.* **26**(7), 769–777 (2012).
17. N. M. Fried and A. L. Burnett, "Novel methods for mapping the cavernous nerves during radical prostatectomy," *Nat. Rev. Urol.* **12**(8), 451–460 (2015).
18. O. Ukimura, C. Magi-Galluzzi, and I. S. Gill, "Real-time transrectal ultrasound guidance during laparoscopic radical prostatectomy: impact on surgical margins," *J. Urol.* **175**(4), 1304–1310 (2006).
19. O. Ukimura and I. S. Gill, "Real-time transrectal ultrasound guidance during nerve sparing laparoscopic radical prostatectomy: pictorial essay," *J. Urol.* **175**(4), 1311–1319 (2006).
20. M. Han, C. Kim, P. Mozer, F. Schäfer, S. Badaan, B. Vigar, K. Tseng, D. Petrisor, B. Trock, and D. Stoianovici, "Tandem-robot assisted laparoscopic radical prostatectomy to improve the neurovascular bundle visualization: a feasibility study," *Urology* **77**(2), 502–506 (2011).
21. O. Ukimura, T. E. Ahlering, and I. S. Gill, "Transrectal ultrasound-guided, energy-free, nerve-sparing laparoscopic radical prostatectomy," *J. Endourol.* **22**(9), 1993–1996 (2008).
22. J. R. Keast, A. M. Booth, and W. C. de Groat, "Distribution of neurons in the major pelvic ganglion of the rat which supply the bladder, colon or penis," *Cell Tissue Res.* **256**(1), 105–112 (1989).
23. D. C. Gray, E. M. Kim, V. E. Coter, A. Bajaj, V. P. Staudinger, C. A. Hehir, and S. Yazdanfar, "Dual-mode laparoscopic fluorescence image-guided surgery using a single camera," *Biomed. Opt. Express* **3**(8), 1880–1890 (2012).
24. L. B. Boyette, M. A. Reardon, A. J. Mirelman, T. D. Kirkley, J. J. Lysiak, J. B. Tuttle, and W. D. Steers, "Fiberoptic imaging of cavernous nerves in vivo," *J. Urol.* **178**(6), 2694–2700 (2007).
25. Q. T. Nguyen and R. Y. Tsien, "Fluorescence-guided surgery with live molecular navigation--a new cutting edge," *Nat. Rev. Cancer* **13**(9), 653–662 (2013).
26. M. A. Whitney, J. L. Crisp, L. T. Nguyen, B. Friedman, L. A. Gross, P. Steinbach, R. Y. Tsien, and Q. T. Nguyen, "Fluorescent peptides highlight peripheral nerves during surgery in mice," *Nat. Biotechnol.* **29**(4), 352–356 (2011).
27. A. Chaux, J. Eifler, S. Karram, T. Al-Hussain, S. Faraj, M. Pomper, R. Rodriguez, and G. J. Netto, "Focal positive prostate-specific membrane antigen (PSMA) expression in ganglionic tissues associated with prostate neurovascular bundle: implications for novel intraoperative PSMA-based fluorescent imaging techniques," *Urol. Oncol.* **31**(5), 572–575 (2013).
28. S. L. Gibbs-Strauss, K. A. Nasr, K. M. Fish, O. Khullar, Y. Ashitate, T. M. Siclovan, B. F. Johnson, N. E. Barnhardt, C. A. Tan Hehir, and J. V. Frangioni, "Nerve-highlighting fluorescent contrast agents for image-guided surgery," *Mol. Imaging* **10**(2), 91–101 (2011).
29. K. C. Lee, S. Sharma, J. B. Tuttle, and W. D. Steers, "Origin and characterization of retrograde labeled neurons supplying the rat urethra using fiberoptic confocal fluorescent microscopy in vivo and immunohistochemistry," *J. Urol.* **184**(4), 1550–1554 (2010).
30. H. H. Davila, M. Mamcarz, I. Nadelhaft, R. Salup, J. Lockhart, and R. E. Carrion, "Visualization of the neurovascular bundles and major pelvic ganglion with fluorescent tracers after penile injection in the rat," *BJU Int.* **101**(8), 1048–1051 (2008).
31. A. K. Tewari, M. M. Shevchuk, J. Sterling, S. Grover, M. Herman, R. Yadav, K. Mudalair, A. Srivastava, M. A. Rubin, W. R. Zipfel, F. R. Maxfield, C. Xu, W. W. Webb, and S. Mukherjee, "Multiphoton microscopy for structure identification in human prostate and periprostatic tissue: implications in prostate cancer surgery," *BJU Int.* **108**(9), 1421–1429 (2011).
32. R. Yadav, S. Mukherjee, M. Hermen, G. Tan, F. R. Maxfield, W. W. Webb, and A. K. Tewari, "Multiphoton microscopy of prostate and periprostatic neural tissue: a promising imaging technique for improving nerve-sparing prostatectomy," *J. Endourol.* **23**(5), 861–867 (2009).
33. L. Gao, H. Zhou, M. J. Thrall, F. Li, Y. Yang, Z. Wang, P. Luo, K. K. Wong, G. S. Palapattu, and S. T. Wong, "Label-free high-resolution imaging of prostate glands and cavernous nerves using coherent anti-Stokes Raman scattering microscopy," *Biomed. Opt. Express* **2**(4), 915–926 (2011).
34. R. Li, E. Phillips, P. Wang, C. J. Goergen, and J. X. Cheng, "Label-free in vivo imaging of peripheral nerve by multispectral photoacoustic tomography," *J. Biophotonics* **9**(1-2), 124–128 (2016).
35. T. P. Matthews, C. Zhang, D. K. Yao, K. Maslov, and L. V. Wang, "Label-free photoacoustic microscopy of peripheral nerves," *J. Biomed. Opt.* **19**(1), 016004 (2014).
36. J. G. Fujimoto, "Optical coherence tomography for ultrahigh resolution in vivo imaging," *Nat. Biotechnol.* **21**(11), 1361–1367 (2003).

37. N. M. Fried, S. Rais-Bahrami, G. A. Lagoda, A. Y. Chuang, L. M. Su, and A. L. Burnett III, "Identification and imaging of the nerves responsible for erectile function in rat prostate, in vivo, using optical nerve stimulation and optical coherence tomography," *IEEE J. Sel. Top. Quantum Electron.* **13**(6), 1641–1645 (2007).
38. N. M. Fried, S. Rais-Bahrami, G. A. Lagoda, Y. Chuang, A. L. Burnett, and L. M. Su, "Imaging the cavernous nerves in the rat prostate using optical coherence tomography," *Lasers Surg. Med.* **39**(1), 36–41 (2007).
39. S. Rais-Bahrami, A. W. Levinson, N. M. Fried, G. A. Lagoda, A. Hristov, Y. Chuang, A. L. Burnett, and L. M. Su, "Optical coherence tomography of cavernous nerves: a step toward real-time intraoperative imaging during nerve-sparing radical prostatectomy," *Urology* **72**(1), 198–204 (2008).
40. M. Aron, J. H. Kaouk, N. J. Hegarty, J. R. Colombo, Jr., G. P. Haber, B. I. Chung, M. Zhou, and I. S. Gill, "Second prize: preliminary experience with the Nirx optical coherence tomography system during laparoscopic and robotic prostatectomy," *J. Endourol.* **21**(8), 814–818 (2007).
41. P. P. Dangle, K. K. Shah, B. Kaffenberger, and V. R. Patel, "The Use of High Resolution Optical Coherence Tomography to Evaluate Robotic Radical Prostatectomy Specimens," *Int. Braz. J. Urol.* **35**(3), 344–353 (2009).
42. S. Chitchian, T. P. Weldon, M. A. Fiddy, and N. M. Fried, "Combined image-processing algorithms for improved optical coherence tomography of prostate nerves," *J. Biomed. Opt.* **15**(4), 046014 (2010).
43. S. Chitchian, M. A. Fiddy, and N. M. Fried, "Denoising during optical coherence tomography of the prostate nerves via wavelet shrinkage using dual-tree complex wavelet transform," *J. Biomed. Opt.* **14**(1), 014031 (2009).
44. S. Chitchian, T. P. Weldon, and N. M. Fried, "Segmentation of optical coherence tomography images for differentiation of the cavernous nerves from the prostate gland," *J. Biomed. Opt.* **14**(4), 044033 (2009).
45. S. Chitchian, M. Fiddy, and N. M. Fried, "Wavelet denoising during optical coherence tomography of the prostate nerves using the complex wavelet transform," in *Proc. of IEEE Engineering in Medicine and Biology*, 3016–3019 (2008).
46. M. Yamanari, S. Makita, V. D. Madjarova, T. Yatagai, and Y. Yasuno, "Fiber-based polarization-sensitive Fourier domain optical coherence tomography using B-scan-oriented polarization modulation method," *Opt. Express* **14**(14), 6502–6515 (2006).
47. C. Hitzenberger, E. Goetzinger, M. Sticker, M. Pircher, and A. Fercher, "Measurement and imaging of birefringence and optic axis orientation by phase resolved polarization sensitive optical coherence tomography," *Opt. Express* **9**(13), 780–790 (2001).
48. M. Yamanari, S. Makita, and Y. Yasuno, "Polarization-sensitive swept-source optical coherence tomography with continuous source polarization modulation," *Opt. Express* **16**(8), 5892–5906 (2008).
49. J. F. de Boer and T. E. Milner, "Review of polarization sensitive optical coherence tomography and Stokes vector determination," *J. Biomed. Opt.* **7**(3), 359–371 (2002).
50. J. F. de Boer, T. E. Milner, M. J. van Gemert, and J. S. Nelson, "Two-dimensional birefringence imaging in biological tissue by polarization-sensitive optical coherence tomography," *Opt. Lett.* **22**(12), 934–936 (1997).
51. B. Cense, T. C. Chen, B. H. Park, M. C. Pierce, and J. F. de Boer, "In vivo depth-resolved birefringence measurements of the human retinal nerve fiber layer by polarization-sensitive optical coherence tomography," *Opt. Lett.* **27**(18), 1610–1612 (2002).
52. B. Cense, T. C. Chen, B. H. Park, M. C. Pierce, and J. F. de Boer, "In vivo birefringence and thickness measurements of the human retinal nerve fiber layer using polarization-sensitive optical coherence tomography," *J. Biomed. Opt.* **9**(1), 121–125 (2004).
53. E. Götzinger, M. Pircher, M. Sticker, A. F. Fercher, and C. K. Hitzenberger, "Measurement and imaging of birefringent properties of the human cornea with phase-resolved, polarization-sensitive optical coherence tomography," *J. Biomed. Opt.* **9**(1), 94–102 (2004).
54. C. E. Saxer, J. F. de Boer, B. H. Park, Y. Zhao, Z. Chen, and J. S. Nelson, "High-speed fiber based polarization-sensitive optical coherence tomography of in vivo human skin," *Opt. Lett.* **25**(18), 1355–1357 (2000).
55. Y. Yasuno, S. Makita, Y. Sutoh, M. Itoh, and T. Yatagai, "Birefringence imaging of human skin by polarization-sensitive spectral interferometric optical coherence tomography," *Opt. Lett.* **27**(20), 1803–1805 (2002).
56. M. C. Pierce, R. L. Sheridan, B. Hyle Park, B. Cense, and J. F. de Boer, "Collagen denaturation can be quantified in burned human skin using polarization-sensitive optical coherence tomography," *Burns* **30**(6), 511–517 (2004).
57. S. M. Srinivas, J. F. de Boer, H. Park, K. Keikhanzadeh, H. E. Huang, J. Zhang, W. Q. Jung, Z. Chen, and J. S. Nelson, "Determination of burn depth by polarization-sensitive optical coherence tomography," *J. Biomed. Opt.* **9**(1), 207–212 (2004).
58. S. K. Nadkarni, M. C. Pierce, B. H. Park, J. F. de Boer, P. Whittaker, B. E. Bouma, J. E. Bressner, E. Halpern, S. L. Houser, and G. J. Tearney, "Measurement of collagen and smooth muscle cell content in atherosclerotic plaques using polarization-sensitive optical coherence tomography," *J. Am. Coll. Cardiol.* **49**(13), 1474–1481 (2007).
59. M. S. Islam, M. C. Oliveira, Y. Wang, F. P. Henry, M. A. Randolph, B. H. Park, and J. F. de Boer, "Extracting structural features of rat sciatic nerve using polarization-sensitive spectral domain optical coherence tomography," *J. Biomed. Opt.* **17**(5), 056012 (2012).
60. F. P. Henry, Y. Wang, C. L. Rodriguez, M. A. Randolph, E. A. Rust, J. M. Winograd, J. F. de Boer, and B. H. Park, "In vivo optical microscopy of peripheral nerve myelination with polarization sensitive-optical coherence tomography," *J. Biomed. Opt.* **20**(4), 046002 (2015).
61. S. Lee, J. H. Lee, J. H. Park, Y. Yoon, W. K. Chung, H. Tchah, M. J. Kim, and K. H. Kim, "In vivo 3D measurement of moxifloxacin and gatifloxacin distributions in the mouse cornea using multiphoton microscopy," *Sci. Rep.* **6**, 25339 (2016).
62. Y. Yoon, Q. Li, V. H. Le, W. H. Jang, T. Wang, B. Kim, S. Son, W. K. Chung, C. Joo, and K. H. Kim, "Dark-field polarization-sensitive optical coherence tomography," *Opt. Express* **23**(10), 12874–12886 (2015).

63. B. H. Park, M. C. Pierce, B. Cense, and J. F. de Boer, "Jones matrix analysis for a polarization-sensitive optical coherence tomography system using fiber-optic components," *Opt. Lett.* **29**(21), 2512–2514 (2004).
64. K. H. Kim, B. H. Park, Y. Tu, T. Hasan, B. Lee, J. Li, and J. F. de Boer, "Polarization-sensitive optical frequency domain imaging based on unpolarized light," *Opt. Express* **19**(2), 552–561 (2011).
65. A. Villers, T. Piechaud, J. Walz, and Y. Butet, "Surgical Anatomy of the Prostate for Radical Prostatectomy," in *Robotic Urology*, H. John, and P. Wiklund, eds. (Springer Berlin Heidelberg, Berlin, Heidelberg, 2013), pp. 187–198.
66. E. G. Zotova, H. H. Schaumburg, C. S. Raine, B. Cannella, M. Tar, A. Melman, and J. C. Arezzo, "Effects of hyperglycemia on rat cavernous nerve axons: a functional and ultrastructural study," *Exp. Neurol.* **213**(2), 439–447 (2008).
67. H. H. Schaumburg, E. Zotova, B. Cannella, C. S. Raine, J. Arezzo, M. Tar, and A. Melman, "Structural and functional investigations of the murine cavernosal nerve: a model system for serial spatio-temporal study of autonomic neuropathy," *BJU Int.* **99**(4), 916–924 (2007).
68. A. A. Sattar, J. C. Noël, J. J. Vanderhaeghen, C. C. Schulman, and E. Wespes, "Prostate capsule: computerized morphometric analysis of its components," *Urology* **46**(2), 178–181 (1995).
69. Y. Yoon, W. H. Jang, P. Xiao, B. Kim, T. Wang, Q. Li, J. Y. Lee, E. Chung, and K. H. Kim, "In vivo wide-field reflectance/fluorescence imaging and polarization-sensitive optical coherence tomography of human oral cavity with a forward-viewing probe," *Biomed. Opt. Express* **6**(2), 524–535 (2015).

1. Introduction

Nerve-sparing radical prostatectomy (NSRP) is a surgical removal procedure of all or part of the prostate capsule containing cancer while preserving nerves affecting a man's erectile function [1]. Cavernous nerves (CNs), which course along the surface of prostate capsule, are responsible for the function [2, 3]. There are risks of injury in CNs during radical prostatectomy, because CNs are located close to the prostate surface. The distance between CNs and prostate surface varies depending on different areas from several hundreds of micrometers to a few centimeters apart. The current method of identifying CNs during NSRP procedure is based on their visual appearance and general understanding of the anatomy [4–10]. An electrophysiological testing method such as electromyographic (EMG) stimulation [11–13] and various imaging methods have been developed and are under investigation to provide better identification of CNs [14–17]. The imaging methods are transrectal ultrasound (TRUS) [18–21], dye-based fluorescence imaging [22–30], multiphoton microscopy (MPM) [31, 32], coherent anti-Stokes Raman scattering (CARS) microscopy [33], and photoacoustic microscopy (PAM) [34, 35]. However, these imaging methods have their own limitations as far as their use for the surgery. Ultrasound imaging method has poor resolutions for visualizing nerves. Fluorescence imaging method relies on exogenous agents for nerve labeling and is limited in clinical applications. MPM and CARS microscopy methods visualized individual nerves, but have limitation in imaging depths down to a few hundred micrometers from the surface as well as small imaging fields of view.

OCT is a 3D imaging technique based on light back reflection, and it can visualize tissue microstructure and vasculature at approximately ten micrometer resolutions down to a few millimeters from the surface in typical tissues in real time [36]. OCT visualizations of CNs have been demonstrated in both rat model [37, 38] and human [39–41]. The previous OCT studies based on structural imaging of CNs in the prostate, and they had difficulties in distinguishing CNs from surrounding tissue compartments due to similarity in morphology. Complementary image processing algorithms, such as segmentation, denoising, and edge detection techniques have been developed for better identification and imaging of the CNs [42–45]. Even with all these developments, it is still challenging to detect CNs based on structural information.

Polarization-sensitive OCT (PS-OCT) is a functional OCT technique providing polarization information of tissue as well as structure [46–50]. PS-OCT is useful for detecting tissues having polarization properties such as birefringence by providing additional contrast for distinction, and has been applied for studying various organs such as eye [51–53], skin [54–57], and coronary artery [58]. Nerves usually express birefringence partially by the microtubule arrangement of nerve axons themselves and their alignment, and by myelin sheath surrounding the nerve axons. Recently, PS-OCT was applied to qualitative detection and quantitative characterization of rat sciatic nerve [59, 60].

In this study, PS-OCT was applied for detection of prostatic nerves in periprostatic tissues by using both structural and birefringent information. PS-OCT imaging was conducted on both rat prostates and human prostatectomy specimens *ex vivo*, and histological analysis with immunofluorescence staining or MPM imaging was conducted for comparison.

2. Materials and methods

2.1 Sample preparations

Experimental procedures in this study were approved by the Institutional Animal Care and Use Committee (IACUC), and the Institutional Review Board (IRB) at the Catholic University of Korea, Seoul St. Mary's Hospital. All experiments were carried out in accordance with the approved guidelines and regulations. 8 male Sprague-Dawley rat prostates and 3 human prostatectomy specimens were used in this study. Rats were anesthetized with subcutaneous injection of Zoletil 50 (Virbac Laboratories, Carros, France) and xylazine hydrochloride (Rompun; Bayer, Seoul, Korea) at dosages of 15 mg/kg and 5 mg/kg respectively. Major pelvic ganglion (MPG) is parasympathetic ganglion on either side of the pelvic plexus, and nerves within this ganglion are projected to three pelvic organs: the penis, colon, and urinary bladder. CNs are post-ganglionic nerves derived from MPG to the penis, and its preservation during NSRP is crucial to prevent erectile dysfunction and complications. MPG and CNs were first identified by visual examination following midline celiotomy, and single 3-0 nylon sutures or medical marking dyes (1003-3 Black, Davidson Marking System, Bradley Products, Inc.) were placed on both sides of MPG and CNs for marking, respectively. Three cases of radical prostatectomy were performed by surgeons from January 2015 to February 2015, and the prostatectomy specimens were imaged immediately after the surgery. A picture of the prostatectomy specimen is shown in Fig. 1. Orientation of the prostatectomy specimen was specified by counterclockwise numbering around the perimeter with reference to the urethral opening as the apex, and 6 o'clock and 12 o'clock were numbered to the posterior and anterior sides, respectively. The prostatic nerves, which course along the posterolateral side of prostate, are known to be in higher density and size [9, 10], and more responsible for erectile function [13] compared to the ones in the anterior side. Three different orientation sites at 3, 5, and 12 o'clock were imaged in individual specimens.

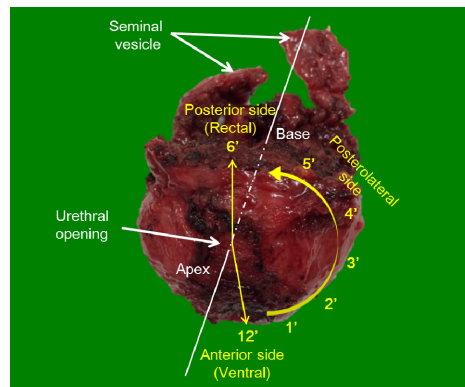


Fig. 1. A picture of radical prostatectomy specimen with orientation. Orientation of the prostatectomy specimen was numbered counterclockwise with respect to the urethral opening, and 12 o'clock and 6 o'clock were numbered to the anterior and posterior sides, respectively.

2.2 Histologic analysis

Following PS-OCT imaging, the rat prostate and human prostatectomy specimens were processed for histological analysis. The specimens were fixed in 4% paraformaldehyde for 24 h at room temperature, embedded with paraffin, and cut into 3 μ m thick sections with a microtome. The paraffin sections were immunostained with the primary antibody neuron-

specific β -III tubulin (diluted 1:200; Abcam, Cambridge, UK). The Alexa Fluor 488 (diluted 1:500; Invitrogen, Carlsbad, USA) secondary antibody was used for signal detection and mounted with DAPI (4,6-diamidino-2-phenylindole; Vector Labs, Burlingame, CA, USA) for nuclei. Digital images were obtained using a Zeiss LSM 510 Meta confocal microscope (Zeiss, Germany).

2.3 Multiphoton microscopy (MPM) imaging

It is difficult to compare histological images with PS-OCT images in order to find spatial co-registration due to the possibility of missing the desired sections during histological processing. In addition, histological images tend to have morphological distortion. In order to make direct comparison, rat prostate specimens which were fixed after PS-OCT imaging were imaged by multiphoton microscopy (MPM, TCS SP5 II, Leica, Germany) with a Ti-Sapphire laser (Chameleon Vision II, Coherent) at 140 fs pulse width and 80 MHz pulse repetition rate. MPM imaging was performed using a $20\times$ objective lens (HCX IRAPO L $20\times$, 1.0NA, water immersion, Leica, Germany) with 1.5 μm z-stepwise and processed by LAS AF Lite (Leica, Germany). In order to enhance fluorescence signal of tissue, moxifloxacin ophthalmic solution (Vigamox, Alcon Laboratories, Fort Worth, US) was topically administered 20 min in 12.4 mM concentration before MPM imaging. It was reported that moxifloxacin can be used as a cell labeling agent for MPM, due to its properties of intrinsic multiphoton fluorescence and high accumulation inside cells [61]. Size of an acquired image was 1024×1024 pixels covering a field of view of $700\text{ }\mu\text{m}\times 700\text{ }\mu\text{m}$, and excitation wavelength was set to 780 nm for fluorophores in moxifloxacin.

2.5. Polarization-sensitive optical coherence tomography (PS-OCT)

All PS-OCT imaging in this study was performed by using a custom-built system, and a schematic of the PS-OCT system is shown in Fig. 2. Detail information of the system was described in a previous report [62]. The light source was a wavelength swept source (SSOCT-1310, AXSUN Technologies) with a center wavelength of 1310 nm, bandwidth of 107 nm, sweeping speed of 50 kHz, and imaging depth range of 6 mm in the air. Two orthogonal polarization states having different optical path lengths were generated by a passive delay unit (PDU). In the sample arm of an interferometer setup, light was collimated to 1.8 mm in diameter with a fiber collimator (HPUCO-13A-1300/1550-S-11AS, OZ optics), and passed a 2D galvano mirror scanner (GVS012, Thorlabs), an 5x objective lens (L, LSM03, Thorlabs), an optical window, and then focused at the sample. The window was slanted at 8° to the normal to avoid collecting strong specular reflection, and it maintained the tissue surface close to the zero optical path length difference by touching. Reflected light from both the sample and reference arms was combined and collected by a polarization diverse setup containing two balanced photodetectors (PDB410C, Thorlabs) in the detection arm. Data was obtained in 3D by acquiring multiple cross-sectional images in the x-z plane with step-wise increment in the y direction. Imaging field was typically 5 mm \times 5 mm in the x and y directions, consisting of 500 pixels \times 500 pixels. Image acquisition time was approximately 0.01 s and 5 s for a 2D cross-sectional image and a 3D image respectively. The signal-to-noise ratio of the system was 103.2 dB. Imaging depth was approximately 1.5 mm in tissue and system resolutions were measured as 20 μm and 10.8 μm in the lateral and axial directions in the air respectively. Data was post-processed to get both intensity OCT and polarization-sensitive (PS) OCT images using MATLAB (Mathworks). PS-OCT images were obtained by analyzing the sample Jones matrices through eigenvector decomposition [63, 64], and accumulated phase retardation was calculated as a function of depth. In PS-OCT images, black and white colors represent 0° and 180° accumulated phase retardation respectively from the surface. En face intensity OCT and PS-OCT images in the x-y plane were generated from 3D reconstructed data set by compiling cross-sectional images using MATLAB.

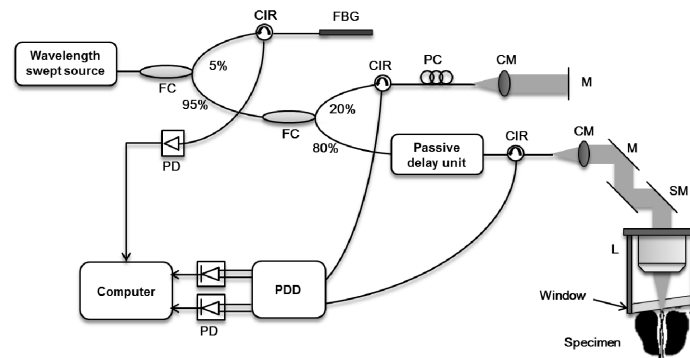


Fig. 2. System configuration of PS-OCT. PC: polarization controller, FBG: fiber Bragg grating, CM: collimator, CIR: fiber circulator, FC: fiber coupler, PBS: polarizing beam splitter, PD: photodetector, PDD: polarization diverse detection, M: mirror, SM: scanning mirror, L: 5x OCT scan lens (EF = 36 mm).

3. Results

3.1. PS-OCT imaging of rat prostate *ex vivo*

PS-OCT imaging was conducted on the rat prostate tissues containing MPG and CNs *ex vivo*, and results are shown in Fig. 3 and Fig. 4, respectively. Both OCT intensity and PS-OCT images are shown in an en face (x-y) plane at a superficial depth and two cross-sectional (x-z) planes, and a histological image of the same sample in the en face plane is presented for comparison. En face OCT intensity and PS-OCT images in Fig. 3(a), 3(b) and Fig. 4(a), 4(b) are at approximately 175 μm and 95 μm deep from the tissue surface, respectively. These depths were calculated by assuming the refractive index of typical biological tissue to be 1.4. Locations of the cross-sections in Fig. 3(c)-3(f) and Fig. 4(c)-4(f) are marked with dashed line I and II in the corresponding en face images. Histological images at the sites of MPG and CNs are shown in Fig. 3(g) and Fig. 4(g), respectively. The prostatic glands and nerves are visualized by DAPI (4, 6-diamidino-2-phenylindole, blue) nucleus staining and neuron-specific β -III tubulin antibody (green) respectively.

PS-OCT images of MPG containing rat prostate tissue visualized various periprostatic structures. Two cross-sectional OCT intensity images show a thin and highly scattering superficial layer covering the prostate, which could be prostate capsule. Below the covering layer, tissues with different morphologies are shown. Weakly scattering compartmented structures with strongly scattering spots are shown in Fig. 3(c), and these structures are fatty tissues. Hexagonal shaped structures are shown in both cross-sections Fig. 3(c) and 3(e), and these are prostatic glands. Cross-sectional PS-OCT images in Fig. 3(d) and 3(f) show local birefringence in some part of the superficial highly scattering layer. Birefringent structures become clearer in en face PS-OCT image at a superficial depth, because the birefringent structures appear in white color out of black background. The birefringent structures in MPG containing prostate tissue are fibrous with many branches which are consistent with morphologies of nerves surrounding MPG, and these birefringent fibrous structures are indicated by arrows (Fig. 3(b)). Presence of MPG in the tissue was confirmed by histology shown in Fig. 3(g). En face OCT intensity image in Fig. 3(a) shows the fatty tissues and prostatic glands clearly but the birefringent fibrous structures are not clearly visible.

PS-OCT images of CN containing rat prostate tissue show similar structures as those of the MPG containing tissue. Cross-sectional OCT intensity and PS-OCT images in Fig. 4(c) and 4(d) shows periprostatic fatty tissues and local birefringence in the highly scattering superficial layer. En face PS-OCT image at a superficial depth in Fig. 4(b) shows birefringent fibrous structures which indicated by arrows. These birefringent fibrous structures could be CNs, since there are no other fibrous structures in periprostatic tissue. Presence of nerves in the same tissue was confirmed by histology shown in Fig. 4(g). Cross-sectional OCT intensity

image in Fig. 4(e) shows the highly scattering superficial layer covering the prostate tissue and relatively large gland structures. Such gland structures appear well in en face OCT intensity image (Fig. 4(a)) as well.

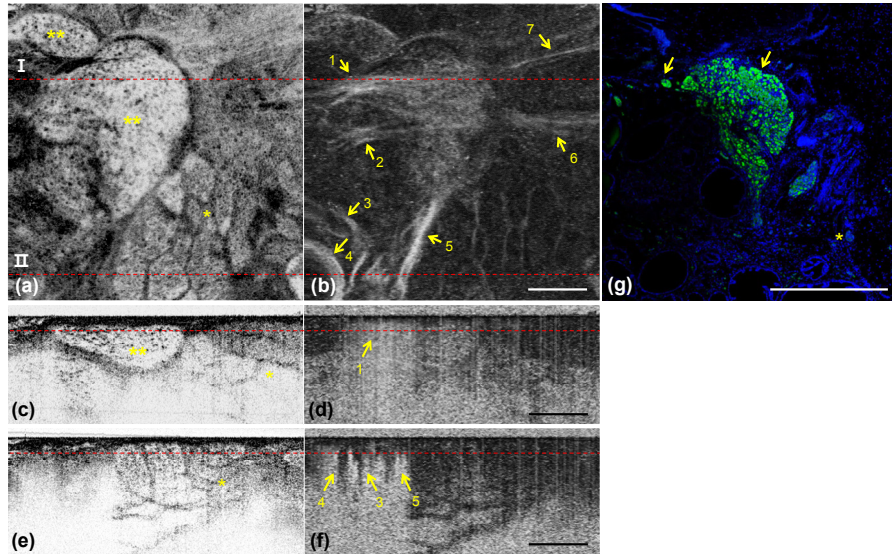


Fig. 3. PS-OCT images and histological images of rat MPG site ex vivo. (a, b) Intensity OCT and PS-OCT images in the en face x-y plane ([Visualization 1](#)) and (c-f) in the cross-sectional x-z planes ([Visualization 2](#)). (g) An immunofluorescence stained histological image. Dashed line I and II indicate locations of the cross-sections (c, d) and (e, f) respectively. A star (*), double stars (**) and arrows indicate periprostic fats, prostatic glands and birefringent fibrous structures, respectively. All scale bars are 1 mm.

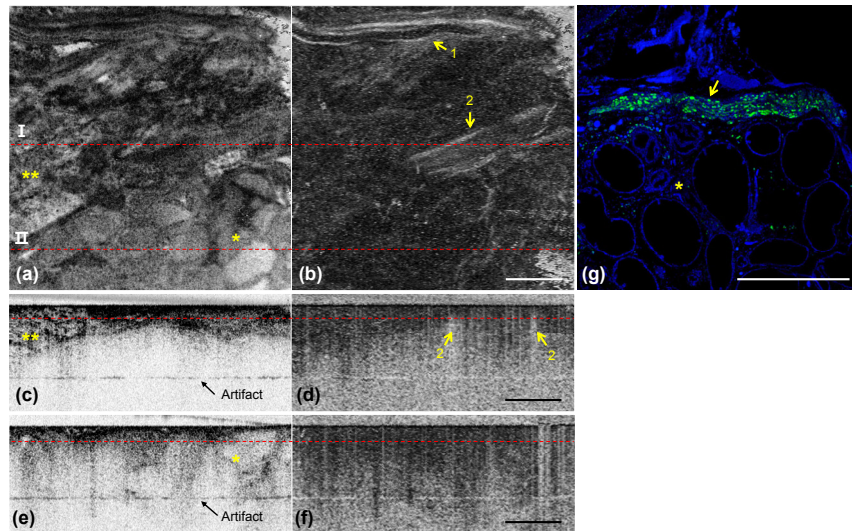


Fig. 4. PS-OCT images and histological images of rat CN site ex vivo. (a, b) Intensity OCT and PS-OCT images in the en face x-y plane ([Visualization 3](#)) and (c-f) in the cross-sectional x-z planes ([Visualization 4](#)). (g) An immunofluorescence stained histological image. Dashed line I and II indicate locations of the cross-sections (c, d) and (e, f) respectively. A star (*), double stars (**) and arrows indicate periprostic fats, prostatic glands and birefringent fibrous structures, respectively. All scale bars are 1 mm.

3.2. Comparison between PS-OCT and MPM imaging of rat prostate ex-vivo

Although histological images provide definite answer about the presence of nerves, it is difficult to find spatial co-registration in between histological images and PS-OCT images due to morphological distortion and possible sectioning error during histological processing. Another way to confirm the findings in PS-OCT images is to compare with MPM images, because MPM can visualize microstructures including nerves in the sample. Both PS-OCT and MPM imaging were conducted on the same rat prostate specimens containing MPG for direct comparison, and results are shown in Fig. 5. En face OCT intensity and PS-OCT images at a depth of approximately 150 μm from the sample surface are shown in Fig. 5(a) and 5(b), respectively. A corresponding en face MPM image is shown in Fig. 5(c). This MPM image is a mosaic image consisting of 18 imaging sections, and was acquired in the boxed region of the en face OCT intensity and PS-OCT images. En face OCT intensity and PS-OCT images show hexagonal shaped prostatic glands in the sample, and additional fibrous structures running on the boundary of prostatic glands, respectively. These birefringent fibrous structures contain multiple fibers. High-resolution MPM mosaic image in the same region shows fibrous prostatic nerves and large prostatic glands in good spatial co-registration with en face PS-OCT image. These prostatic nerves, shown in en face MPM image, are mostly approximately $100 \pm 36 \mu\text{m}$ in thickness. Prostatic glands next to the nerves contain multiple round microstructures. En face MPM mosaic image showing the prostatic nerves is at approximately 50 μm deep from the surface, which is different from the depth location of corresponding en face OCT intensity and PS-OCT images. En face PS-OCT image may show birefringent fibrous structures at the higher depth, partly because it displays the accumulated phase retardation with depth from the surface. Since en face PS-OCT image shows good spatial correlation with en face MPM mosaic image, birefringent and fibrous structure found in PS-OCT image was confirmed to be prostatic nerves.

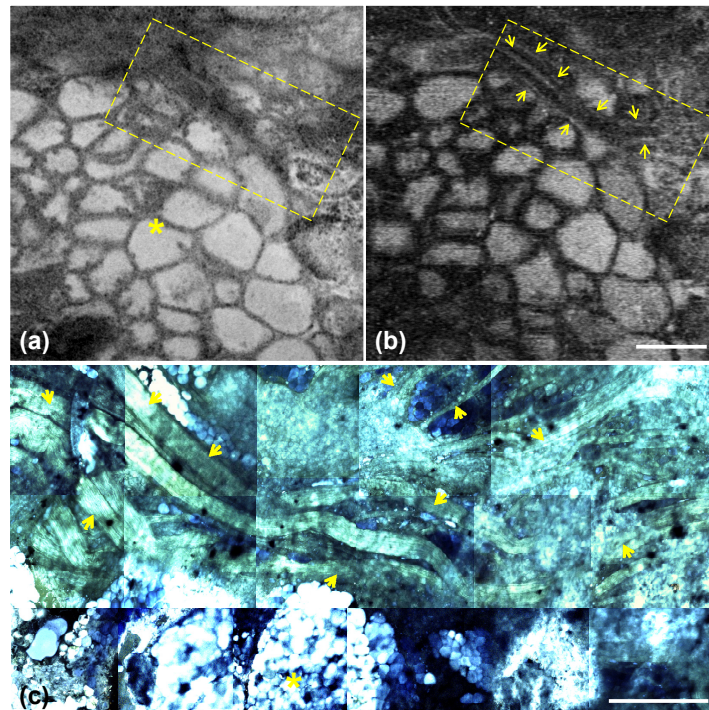


Fig. 5. PS-OCT images and mosaic MPM image of rat periprostatic nerves surrounding MPG ex vivo. (a, b) Intensity OCT and PS-OCT images in the en face x-y plane. Scale bar is 1 mm. (c) Mosaic MPM image consisting of 18 images in dashed box region in (a, b). Scale bar is 500 μm . A star (*) and arrows indicate prostatic glands and nerves, respectively.

3.3 PS-OCT imaging of human prostatectomy specimens *ex vivo*

PS-OCT imaging was conducted on human prostatectomy specimens *ex vivo*, and results of one specimen at different orientations are shown in Fig. 6–Fig. 8. Different from the rat prostate, the human prostate is covered with multiple sheets of connective fibers, called as fascia. Fascia covers the prostate glands and forms periprostatic environment. Prostatic nerves and blood vessels forming neurovascular bundle (NVB) are situated in the space of fascia, and surgeons dissect the interfascial planes during NSRP. NVBs are usually distributed more in the posterolateral side of prostate, and less in the anterior side of prostate [9, 10]. Three different sites of the prostatectomy specimens indicated in Fig. 1 were imaged: 5 and 3 o'clock sites in the posterolateral side, and 12 o'clock site in the anterior side. The results of one representative prostatectomy specimen at 5, 3, and 12 o'clock sites are shown in Fig. 6, Fig. 7 and Fig. 8 respectively. These figures have the same configuration of PS-OCT images as the ones of rat prostate specimens in Fig. 3 and Fig. 4: OCT intensity and PS-OCT images with area of 5 mm x 5 mm in a en face plane (x-y) and two different cross-sectional planes (x-z). En face images shown in Fig. 6(a), 6(b), Fig. 7(a), 7(b) and Fig. 8(a), 8(b) are approximately at 95 μm , 285 μm , and 265 μm deep from the surface, respectively. These depths were calculated by assuming the refractive index of typical biological tissue to be 1.4. Locations of cross-sections in Fig. 6(c)–6(f), Fig. 7(c)–7(f) and Fig. 8(c)–8(f) are marked with dashed line I and II in the corresponding en face images.

Cross-sectional OCT intensity images of the human prostatectomy specimen at 5 o'clock show fatty tissues in Fig. 6(c), and highly scattering superficial layer with underlying fatty tissues in Fig. 6(e). These structures appear different in en face OCT intensity image at a superficial depth: fatty tissue region and relatively uniform region are in the upper and lower halves of the image. Cross-sectional PS-OCT images show local birefringence in the superficial highly scattering layer in Fig. 6(f). En face PS-OCT image at the depth show birefringent fibrous structures indicated by arrows. These birefringent fibrous structures are located on the boundary of the two different regions in en face OCT intensity image. Prostatic glands are not detected by PS-OCT imaging due to relatively thick covering layers of the human prostate compared to the ones in rat prostate.

Cross-sectional OCT intensity images of the human prostatectomy specimen at 3 o'clock show layered tissue structures in both cross-sections in Fig. 7(c) and 7(e). Corresponding cross-sectional PS-OCT images show local birefringence in Fig. 7(d) and uniform birefringence in Fig. 7(f). En face PS-OCT image at superficial depth shows both birefringent fibrous and birefringent sheet-like structures which indicated by arrows and arrow heads respectively. These birefringent structures could be nerves and fascia respectively. Histology of the same tissue shown in Fig. 7(g) confirmed the presence of nerves. En face OCT intensity image at the depth show birefringent fibrous structures on the border between the region of layered structures and fatty tissue.

Cross-sectional PS-OCT images of the human prostatectomy specimen at 12 o'clock show sheet-like structures having uniform birefringence in both cross-sections in Fig. 8(d) and 8(f). These birefringent sheet-like structures indicated by arrow heads, appear clearly in en face PS-OCT image (Fig. 8(b)), and these could be fascia shown in PS-OCT image at 3 o'clock side. Other than the birefringent sheet-like structure, birefringent fibrous structures are not shown in these PS-OCT images at 12 o'clock. Histology of the same tissue in Fig. 8(g) confirmed absence of nerves.

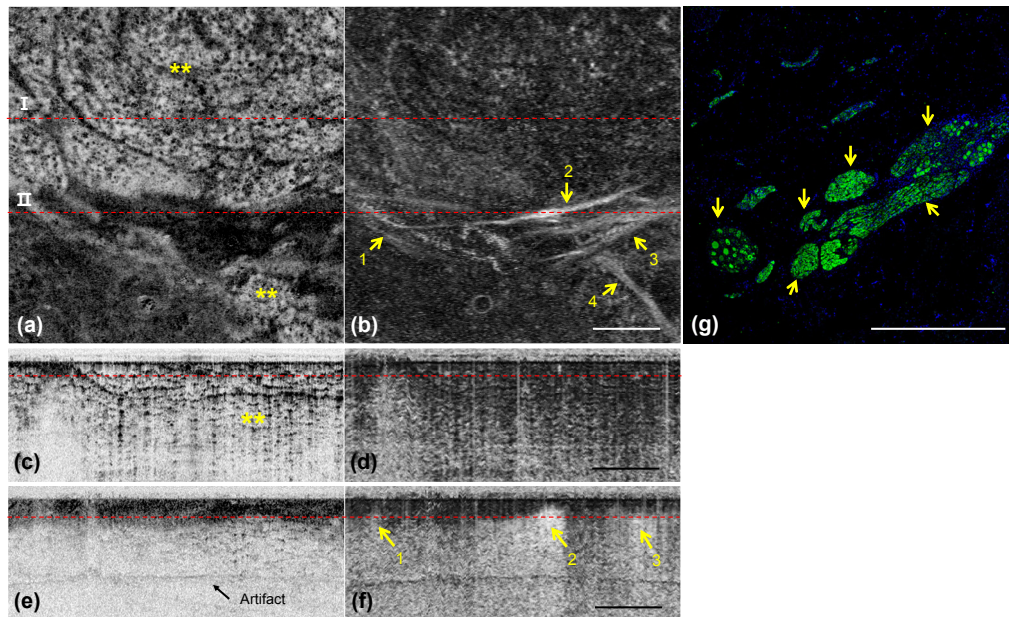


Fig. 6. PS-OCT images and histological images of the human prostatectomy specimen at 5 o'clock site. (a, b) Intensity OCT and PS-OCT images in the en face x-y plane ([Visualization 5](#)) and (c-f) in the cross-sectional x-z plane ([Visualization 6](#)). (g) An immunofluorescence stained histological image. Dashed line I and II indicate locations of the cross-sections (c, d) and (e, f) respectively. Double stars (**) and arrows indicate periprostatic fats and birefringent fibrous structures respectively. All scale bars are 1 mm.

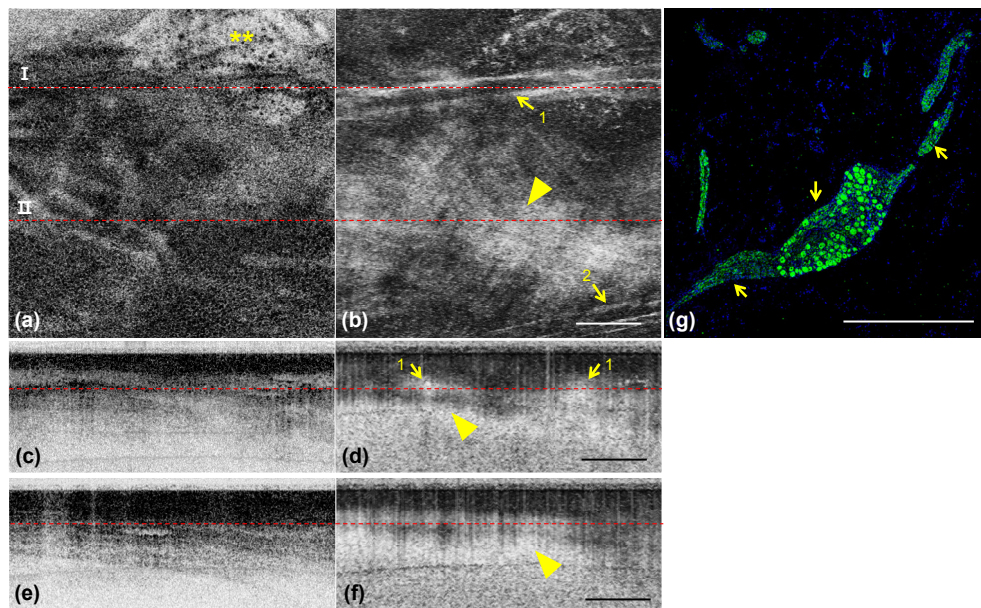


Fig. 7. PS-OCT images and histological images of the human prostatectomy specimen at 3 o'clock site. (a, b) Intensity OCT and PS-OCT images in the en face x-y plane ([Visualization 7](#)) and (c-f) in the cross-sectional x-z plane ([Visualization 8](#)). (g) An immunofluorescence stained histological image. Dashed line I and II indicate locations of the cross-sections (c, d) and (e, f) respectively. Double stars (**), arrows and arrow heads indicate periprostatic fats, birefringent fibrous structures and birefringent sheet-like structures, respectively. All scale bars are 1 mm.

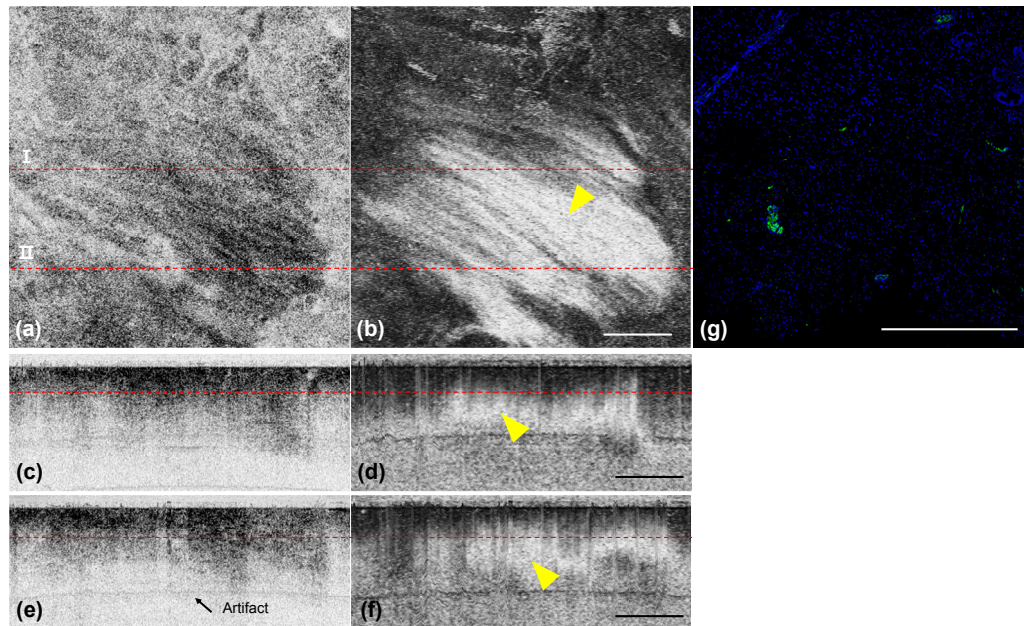


Fig. 8. PS-OCT images and histological images of the human prostatectomy specimen at 12 o'clock site. (a, b) Intensity OCT and PS-OCT images in the en face x-y plane ([Visualization 9](#)) and (c-f) in the cross-sectional x-z plane ([Visualization 10](#)). (g) An immunofluorescence stained histological image. Dashed line I and II indicate locations of the cross-sections (c, d) and (e, f) respectively. Arrow heads indicate birefringent sheet-like structures. All scale bars are 1 mm.

3.4 Various OCT intensity and PS-OCT images of rat and human prostatic nerves

PS-OCT imaging was conducted on 8 rat prostates and 3 human prostatectomy specimens in total, and approximately 2 - 3 different sites were imaged on each sample or sample orientation. In order to show morphological variation, 5 representative en face OCT intensity and PS-OCT images of rat prostates and human prostatectomy specimens showing birefringent fibrous structures are presented in Fig. 9(a)-9(e) and 9(f)-9(j) respectively. Depths of all these en face images were range between 140 – 280 μm from the surface. These depths were calculated by assuming the refractive index of typical biological tissue to be 1.4. En face OCT intensity images show prostatic glands and periprostatic fats by similar morphologies with previous results. En face PS-OCT images showed various birefringent fibrous structures, and there appears to be variation in morphology: some birefringent structures are thin and parallel each other with some space in between (Fig. 9(g) and 9(h)), and others are densely clustered (Fig. 9(b) and 9(c)). Approximately 2 – 5 birefringent fibrous structures were detected in individual en face PS-OCT images on average, and their thickness was 100 – 400 μm in both rat and human prostates. The size of smallest nerves which were detected by PS-OCT was approximately 53 μm and 154 μm in rat and human prostates respectively.

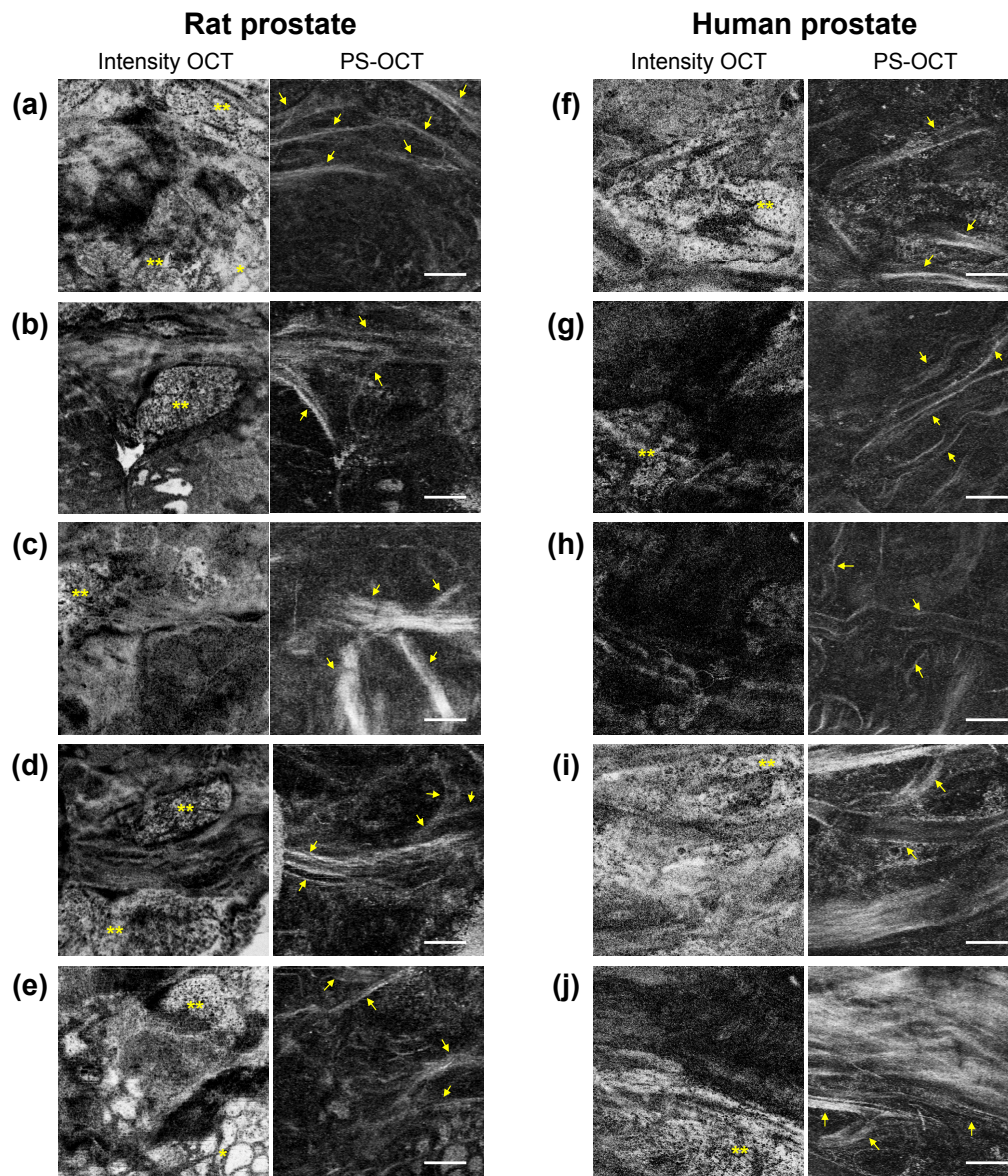


Fig. 9. Various PS-OCT images of rat and human prostatic nerves in the en face (x-y) plane. (a-e) Rat prostates and (f-j) human prostates. A star (*) and double stars (**) indicate prostatic glands and periprostatic fats respectively. Arrows indicate the birefringent fibrous structures of nerves. All scale bars are 1 mm.

4. Discussions

In this study, we investigated the feasibility of PS-OCT imaging for detecting prostatic nerves from surrounding other periprostatic tissues based on both structural and birefringent information. PS-OCT imaging was conducted on 8 rat prostates and 3 human prostatectomy specimens in total, and PS-OCT results were compared with histology or MPM for confirmation. PS-OCT images of rat prostates visualized highly scattering and birefringent fibrous structures at the superficial region. These birefringent and fibrous structures were confirmed to be prostatic nerves by both histology and MPM image. The birefringent fibrous

structures in PS-OCT images could be either individual large nerves or clusters of multiple nerves.

PS-OCT imaging of human prostatectomy specimens were more difficult than the rat tissues, due to thick periprostatic fats covering the prostate capsule, coagulated bloods, and burned resection margin of surgery. These factors could degrade the quality of PS-OCT images. However, PS-OCT images of human prostatectomy specimens visualized fibrous birefringent structures superficially-distributed birefringent sheet-like structures. Different from the rat prostate, human prostatectomy specimens are covered with fascias which have birefringent properties as well. The thickness of fascias is not uniform and varies depending on different sections and patients [65]. Prostatic nerves and fascias could be distinguishable based on morphology in the en face PS-OCT images: fibrous and sheet-like structures respectively.

There were some small nerves, which appeared in MPM image only but not in PS-OCT image, in the rat prostate specimens. Width of those small nerves was approximately 4 - 10 μm in MPM images. This might be because the accumulated phase retardation in those nerves was insufficient for detection by PS-OCT due to either small thickness or weak polarization property. Birefringent property of nerves is from two sources: microtubule arrangement of nerve axons themselves and their alignment, and myelin sheath surrounding the nerve axons. The prostatic nerves consist of both myelinated and unmyelinated nerve fibers and their composition varies on different sections [66, 67]. Therefore, both sources might contribute to birefringence in the prostatic nerves.

In rat prostate, OCT intensity images visualized various periprostatic structures: the prostate capsule at superficial depth, and fat and prostate glands below the prostate capsule. The prostate capsule consists of dense connective tissue rich in elastic fiber and smooth muscle cells, and its thickness varies depending on different areas due to the variations in the volume of smooth muscle content. The mean thickness of human prostate capsule is 0.5 mm to 2 mm [68], and the thickness of rat prostate capsule might be thinner than the human one. The human prostate capsule could not be visualized in OCT intensity images of prostatectomy specimens due to thick periprostatic fats and fascias covering the capsule.

The next step will be pre-clinical study with animal models. For that, the current system will be miniaturized for in-vivo imaging of rat model or for translating PS-OCT as an imaging guide during NSRP by implementing a laparoscopic OCT probe which can do both wide-field imaging and PS-OCT [69]. Also, real-time PS-OCT displaying technique in both cross-sectional and en face views will be developed for rapid nerve detection during surgery. We expect that this study provides a basis of the intraoperative use of PS-OCT for detecting the prostatic nerves, and also it may improve the complete cancer resection while preserving the nerves during any surgeries as well as radical prostatectomy.

Funding

This research was supported in part by Engineering Research Center grant (No. 2011-0030075) and Korea-Sweden Research Cooperation Programme (No. NRF-2014R1A2A1A12067510) of the National Research Foundation (NRF) funded by the Korean government (MEST) and Industrial Technology Innovation Program (No. 10048358) funded by the Ministry Of Trade, Industry & Energy (MI, Korea).

Acknowledgments

We would like to thank Bumju Kim, Taejun Wang, Jun Ho Lee, Seunghun Lee, Calvin J. Yoon, Viet-Hoan Le, Gilgu Lee, Uk Jegal and Soonjae Kwon for technical assistances and helpful discussions.